

# Chapter 5

## Introduction to Causal Dynamical Triangulations

Andrzej Görlich

**Abstract** The method of causal dynamical triangulations is a non-perturbative and background-independent approach to quantum theory of gravity. In this review we present recent results obtained within the four dimensional model of causal dynamical triangulations. We describe the phase structure of the model and demonstrate how a macroscopic four-dimensional de Sitter universe emerges dynamically from the full gravitational path integral. We show how to reconstruct the effective action describing scale factor fluctuations from Monte Carlo data.

### 5.1 Introduction

The model of causal dynamical triangulations (CDT) was proposed some years ago by J. Ambjørn, J. Jurkiewicz and R. Loll with the aim of defining a lattice formulation of quantum gravity from first principles [1–4]. The foundation of this model is the formalism of path integrals applied to quantize a theory of gravitation. The causal dynamical triangulations method is a natural generalization of discretization procedure, introduced in the definition of quantum mechanical Feynman’s path integral, to higher dimensions. In the path integral formulation of quantum gravity, the role of a particle trajectory is played by the geometry of four-dimensional spacetime. CDT provide an explicit recipe for calculating the path integral and for specifying the class of virtual geometries which should be superimposed in the path integral. Let us emphasize that no *ad hoc* discreteness of space-time is assumed from the outset, and the discretization appears only as a regularization, which is intended to be removed in the continuum limit. The presented approach has the virtue that it allows quantum gravity to be relatively easily represented and studied by computer simulations.

Classical theory of gravitation, general relativity, in contrast with other known interactions describes the dynamics of space-time geometry where the considered degree of freedom is the geometry associated with the metric field  $g_{\mu\nu}(x)$ . The non-

---

A. Görlich (✉)

Niels Bohr Institute, University of Copenhagen, Blegdamsvej 17, 2100 Copenhagen, Denmark  
e-mail: [goerlich@nbi.dk](mailto:goerlich@nbi.dk)

vanishing curvature of the underlying space-time geometry is interpreted as a gravitational field. The starting point for construction of the quantum theory of gravitation is the classical Einstein–Hilbert action ( $\{-, +, +, +\}$  signature and sign convention as in [5, 6])

$$S_{\text{EH}}[g_{\mu\nu}] = \frac{1}{16\pi G} \int_{\mathcal{M}} d^4x \sqrt{-\det g} (R - 2\Lambda), \quad (5.1)$$

where  $G$  and  $\Lambda$  are respectively the Newton’s gravitational constant and the cosmological constant,  $\mathcal{M}$  is the space-time manifold equipped with a pseudo-Riemannian metric  $g_{\mu\nu}$  with Minkowskian signature  $\{-, +, +, +\}$  and  $R$  denotes the associated Ricci scalar curvature [7, 8]. We used the natural Planck units  $c = \hbar = 1$ . For simplicity, we assume that the topology of  $\mathcal{M}$  is  $S^1 \times S^3$ .

Path-integrals are one of the most important tools used for the quantization of classical field theories. The path integral or partition function of quantum gravity is defined as a formal integral over all space-time geometries, i.e., equivalence classes of space-time metrics  $g$  with respect to the diffeomorphism group  $\text{Diff}_{\mathcal{M}}$  on  $\mathcal{M}$ , also called histories,

$$Z = \int \mathcal{D}_{\mathcal{M}}[g] e^{iS_{\text{EH}}[g]}. \quad (5.2)$$

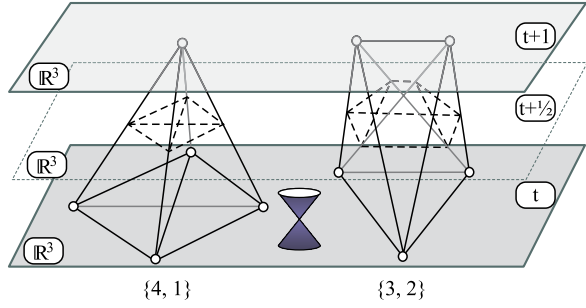
### 5.1.1 Causal Triangulations

To make sense of the formal gravitational path integral (5.2), the causal dynamical triangulations model uses a standard method of regularization, and replaces the path integral over geometries by a sum over a discrete set  $\mathbb{T}$  of all causal triangulations  $\mathcal{T}$ . In other words, CDT serve as a regularization of smooth space-time histories present in the formal path integral (5.2) with piecewise linear manifolds.

The building blocks of four dimensional CDT are four-simplices. A simplex is a generalization of a triangle, which itself is a two-dimensional simplex, to higher dimensions. Each four-dimensional simplex is composed of five vertices connected to each other and is taken to be a subset of a four-dimensional Minkowski space-time together with its inherent light-cone structure. Thus the metric inside every simplex is flat. Figure 5.1 presents a visualization of four-simplices together with a light-cone sketch. A four-dimensional simplicial manifold, with a given topology, is obtained by properly gluing pairwise four-simplices along common tetrahedral faces. A simplicial manifold takes over a metric from simplices of which it is built. In general, such  $n$ -dimensional complex cannot be embedded in  $\mathbb{R}^n$ , which signifies a non-vanishing curvature. The curvature is singular and localized on the triangles.

The underlying assumption of CDT is the causality condition. It has a significant impact on desirable properties of the theory. As a consequence of the original Lorentzian signature of space-time, in a gravitational path integral one should sum over causal geometries only. We will consider only globally hyperbolic pseudo-Riemannian manifolds which allow introducing a global proper-time foliation. The

**Fig. 5.1** A visualization of fundamental building blocks of four-dimensional causal dynamical triangulations: four-simplices. The simplices join two successive slices  $t$  and  $t + 1$ , and are divided into two types:  $\{4, 1\}$  and  $\{3, 2\}$ . The simplices are equipped with the flat Minkowski metric imposing the light-cone structure



leaves of the foliation are spatial three-dimensional Cauchy surfaces  $\Sigma$  and are called *slices*. Because topology changes of the spatial slices are often associated with causality violation, we forbid the topology of the leaves to alter in time. Figure 5.2 illustrates a triangulation with imposed a foliation violating the causality condition. For simplicity, we choose the spatial slices to have a fixed topology  $\Sigma = S^3$ , that of a three-sphere, and establish periodic boundary conditions in the time direction. Therefore, we assume space-time topology to be  $\mathcal{M} = S^1 \times S^3$ , where  $S^1$  corresponds to time and  $S^3$  to space. The spatial slices are enumerated by a discrete *time* coordinate  $i$ . At each integer proper-time step  $i$ , a spatial slice itself forms a triangulation of  $S^3$ , made up of equilateral tetrahedra with a side length  $a_s > 0$ , with an induced metric which has a Euclidean signature. Each vertex lies in one spatial slice and is assigned the corresponding discrete time coordinate  $i$ .

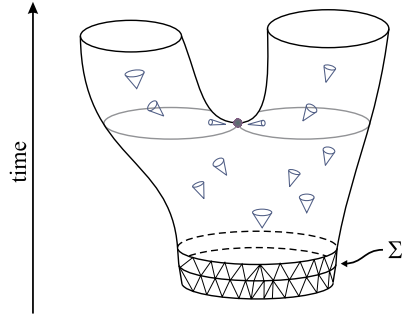
Two successive slices, given respectively by triangulations  $\mathcal{T}^{(3)}(t)$  and  $\mathcal{T}^{(3)}(t + 1)$ , are connected with four-simplices. The simplices are joined in such a way that they form a four-dimensional piecewise linear geometry. Such an object takes the form of a four-dimensional *slab* with the topology of  $[0, 1] \times S^3$  and has  $\mathcal{T}^{(3)}(t)$  and  $\mathcal{T}^{(3)}(t + 1)$  as the three-dimensional boundaries. A set of slabs glued one after another builds the whole simplicial complex. Such connection of two consecutive slices, by interpolating the *space* between them with properly glued four-simplices, does not spoil the *causal structure*. The triangulation of the later slice wholly lies in the future of the earlier one.

Because each simplex connects two consecutive spatial slices and contains vertices lying in both of them, there are four kinds of simplices, namely  $\{1, 4\}$ ,  $\{2, 3\}$ ,  $\{3, 2\}$  and  $\{4, 1\}$ . The first number denotes the number of vertices lying in slice  $\mathcal{T}^{(3)}(t)$ , and the second lying in slice  $\mathcal{T}^{(3)}(t + 1)$ . Figure 5.1 illustrates four-simplices of type  $\{4, 1\}$  and  $\{3, 2\}$  connecting slices  $t$  and  $t + 1$ .

Similarly, due to the causal structure, we distinguish two types of edges. The space-like links connecting two vertices in the same slice have length  $a_s > 0$ . The time-like links connecting two vertices in adjacent slices have length  $a_t$ . In causal dynamical triangulations, the lengths  $a_s$  and  $a_t$  are constant but not necessarily equal. Let us denote the asymmetry factor between the two lengths by  $\alpha$ :

$$a_t^2 = \alpha a_s^2. \tag{5.3}$$

**Fig. 5.2** A visualization of a two-dimensional triangulation with a light-cone structure and a branching point marked. In causal dynamical triangulations spatial slices are not allowed to split, which prevents singularities of the time arrow



In the Lorentzian case  $\alpha < 0$ . The volumes and angles of simplices are functions of  $a_s$  and  $a_t$  and differ for the two types  $\{4, 1\}$  and  $\{3, 2\}$ . Because no coordinates are introduced, the CDT model is manifestly diffeomorphism-invariant. Such a formulation involves only geometric invariants such as lengths and angles.

### 5.1.2 The Regge Action and the Wick Rotation

The Einstein–Hilbert action (5.1) has a natural realization on piecewise linear manifolds called the Regge action. Let  $N_{41}$  mean the number of simplices of type  $\{1, 4\}$  or  $\{4, 1\}$ , and  $N_{32}$  the number of simplices of type  $\{2, 3\}$  or  $\{3, 2\}$ . They sum up to the total number of simplices,  $N_4 = N_{41} + N_{32}$ . The total physical four-volume  $\int_{\mathcal{T}} d^4x \sqrt{|\det g|}$  is given by a linear combination of  $N_{41}$  and  $N_{32}$ . Similarly, the global curvature  $\int_{\mathcal{T}} d^4x \sqrt{|\det g|} R$  can be expressed using the angle deficits which are localized at triangles, and is a linear function of total volumes  $N_{32}$ ,  $N_{41}$  and the total number of vertices  $N_0$ . The Regge action, i.e., action (5.1) calculated for a causal triangulation  $\mathcal{T}$ , can be written in a very simple form,

$$S[\mathcal{T}] \equiv -K_0 N_0[\mathcal{T}] + K_4 N_4[\mathcal{T}] + \Delta(N_{41}[\mathcal{T}] - 6N_0[\mathcal{T}]), \quad (5.4)$$

where  $K_0$ ,  $K_4$  and  $\Delta$  are bare coupling constants, and are nonlinear functions of parameters appearing in the continuous Einstein–Hilbert action, namely  $G$  and  $\Lambda$ , and the asymmetry factor  $\alpha = a_t^2/a_s^2$  which is a regularization parameter [3].  $K_4$  plays a similar role as a cosmological constant, it controls the total volume.  $K_0$  may be viewed as the inverse of the gravitational coupling constant  $G$ .  $\Delta$  is related to the asymmetry factor  $\alpha$  between lengths time-like and spatial-like links. It is zero when  $a_t = a_s$  and does not occur in the Euclidean dynamical triangulations [9].  $\Delta$  will play an important role since a change in  $\Delta$  will be associated with geometric phase transitions which might determine the ultraviolet limit of the lattice theory.

Causal dynamical triangulations provide a regularization of histories appearing in the formal gravitational path integral (5.2). The integral is now discretized by

replacing it with a sum over the set of all causal triangulations  $\mathbb{T}$  weighted with the Regge action (5.4), providing a meaningful definition of the partition function,

$$Z \equiv \sum_{\mathcal{T} \in \mathbb{T}} \frac{1}{C_{\mathcal{T}}} e^{iS[\mathcal{T}]}. \quad (5.5)$$

$C_{\mathcal{T}}$  is the order of the automorphism group of a triangulation  $\mathcal{T}$ , and might be viewed as the remnant of the division by the volume of the diffeomorphism group  $\text{Diff}_{\mathcal{M}}$ .

The advantage of the CDT approach is that for a fixed size of the triangulations, understood as the number of simplices  $N_4$ , the number of combinations is finite, which in general makes it possible to use numerical calculations. Nonetheless, this number grows exponentially with the size. Because of the oscillatory behavior of the integrand (5.5), we are still led into problems in defining the path integral, and in addition the mentioned numerical techniques are not useful. We may evade this problem by applying a trick called Wick rotation, which, roughly, is based on the analytical continuation of the time coordinate to imaginary values, and results in the change of the space-time signature from Lorentzian to Euclidean and a substitution of the complex amplitudes by real probabilities,

$$e^{iS^{\text{Lor}}} \rightarrow e^{-S^{\text{Euc}}}. \quad (5.6)$$

Due to the global proper-time foliation, the Wick rotation is well defined. It can be simply implemented by analytical continuation of the lengths of all time-like edges,  $a_t \rightarrow ia_t$ ,

$$a_t^2 = \alpha a_s^2, \quad \alpha > 0.$$

This procedure is possible, because we have a distinction between time-like and space-like links. The Regge action rotated to the Euclidean sector, after the redefinition applied in (5.6),  $S^{\text{Euc}} = -iS^{\text{Lor}}$ , has exactly the same simple form as its original Lorentzian version (5.4). An exact derivation of the Wick-rotated Regge action can be found in [3].

As a consequence of the regularization procedure and Wick rotation to the Euclidean signature, the partition function (5.2) is finally written as a real sum over the set of all causal triangulations  $\mathbb{T}$ ,

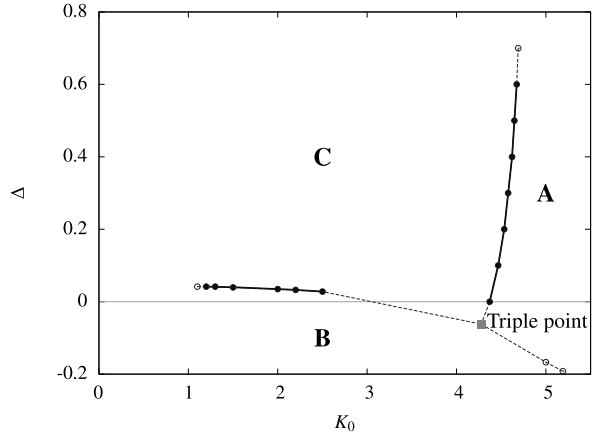
$$Z = \sum_{\mathcal{T} \in \mathbb{T}} \frac{1}{C_{\mathcal{T}}} e^{-S[\mathcal{T}]}. \quad (5.7)$$

We should keep in mind that the Euclidean Regge action  $S[\mathcal{T}]$  and the partition function  $Z$  depend on bare coupling constants  $K_0$ ,  $K_4$  and  $\Delta$ . With the partition function (5.7) there is associated a probability distribution on the space of triangulations  $P[\mathcal{T}]$  which defines the quantum expectation value

$$\langle \mathcal{O} \rangle \equiv \sum_{\mathcal{T} \in \mathbb{T}} \mathcal{O}[\mathcal{T}] P[\mathcal{T}], \quad P[\mathcal{T}] \equiv \frac{1}{Z} \frac{1}{C_{\mathcal{T}}} e^{-S[\mathcal{T}]}, \quad (5.8)$$

where  $\mathcal{O}[\mathcal{T}]$  denotes some observable defined on  $\mathbb{T}$ . The above partition function defines a statistical mechanical problem which is free of oscillations and may be

**Fig. 5.3** A sketch of the phase diagram of the four-dimensional causal dynamical triangulations. The phases correspond to regions on the bare coupling constant  $K_0$ - $\Delta$  plane. We observe three phases: a *crumpled* phase A, a *branched polymer* phase B and the most interesting genuinely four-dimensional de Sitter phase C



tackled in an approximate manner using Monte Carlo methods. Equation (5.7) is the starting point for computer simulations which further allow us to measure expectation values defined by (5.8) and to obtain physically relevant information.

## 5.2 Phase Diagram

The standard version of the causal dynamical triangulations model uses the Regge action (5.4), which depends on a set of three bare coupling constants  $K_0$ ,  $\Delta$  and  $K_4$ . For simulation-related technical reasons it is preferable to keep the total four-volume fluctuating around some finite prescribed value during Monte Carlo simulations. The number of configurations grows exponentially with the size, but the contribution to the partition function coming from extremely large configurations is suppressed by the term involving  $K_4$ . A value of  $K_4$  below the critical value would make the partition function ill defined. Thus  $K_4$ , acting as Lagrange multiplier, needs to be tuned to its critical value, and effectively does not appear as a coupling constant. The two remaining bare coupling constants  $K_0$  and  $\Delta$  can be freely adjusted and depending on their values we observe three qualitatively different behaviors of a typical configuration. The phase structure was first qualitatively described in a comprehensive publication [2] where three phases were labeled A, B and C. The first real phase diagram obtained due to large-scale computer simulations was described in [15]. The phase diagram, based on Monte Carlo measurements, is presented in Fig. 5.3. The solid lines denote observed phase-transition points for configurations of size 8,000 simplices, while the dotted lines represent an interpolation.

In the remainder of this section we describe the properties of the phases and discuss the phase transitions.

- **Phase A.** For large values of  $K_0$  (cf. Fig. 5.3) the universe disintegrates into uncorrelated irregular sequences of maxima and minima with time extent of few

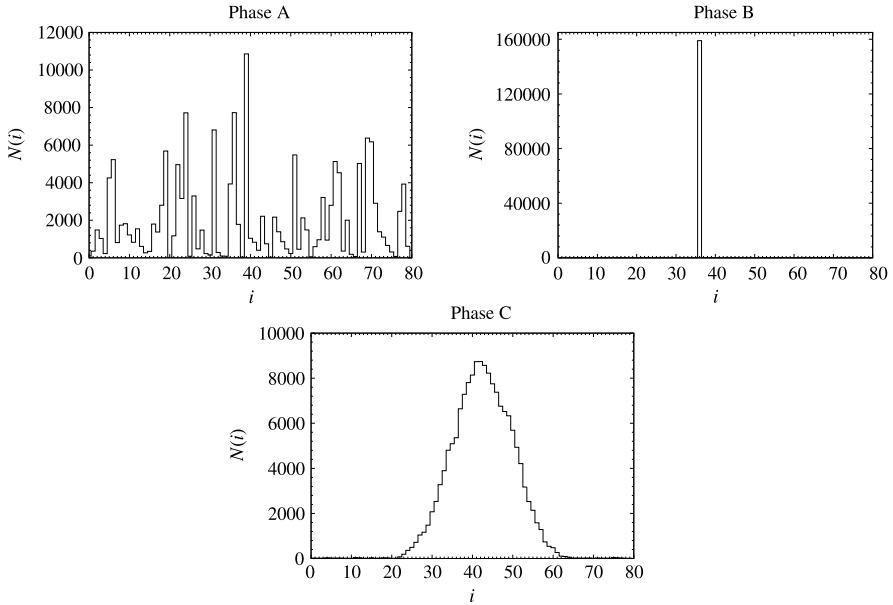


**Fig. 5.4** Snapshot of a spatial volume  $N(i)$  for a typical configuration of phase A, B and C. A typical configuration in phase C is bell-shaped with well-defined spatial and time extent

steps. As an example of a configuration in this phase, the spatial volume distribution  $N(i)$ , defined as the number of tetrahedra in a spatial slice labeled by a discrete time index  $i$ , is shown in Fig. 5.4. When looking along the time direction, we observe a number of small universes. The geometry appears to be oscillating in the time direction. They can merge and split with the passing of the Monte Carlo time. These universes are connected by *necks* not much larger than the smallest possible spatial slice. In the computer algorithm we do not allow these necks to *vanish* such that the configuration becomes disconnected. This phase is related to so-called *branched polymers phase* present in Euclidean dynamical triangulations (EDT) [9]. No spatially- nor time-extended universe, like the universe we see in reality, is observed and phase A is regarded as non-physical.

- **Phase B.** For small values of  $\Delta$  nearly all simplices are localized on one spatial slice. Although we have a large three-volume collected at one spatial hypersurface of a topology of a three-sphere  $S^3$ , the corresponding slice has almost no spatial extent. The Hausdorff dimension is very high, if not infinite. In the case of infinite Hausdorff dimension the universe has neither time extent nor spatial extent, there is no geometry in a traditional sense. Phase B is also regarded as non-physical.
- **Phase C.** For larger values of  $\Delta$  we observe the third, physically most interesting, phase. In this range of bare coupling constants, a typical configuration is bell-shaped and behaves like a well-defined four-dimensional manifold (cf. Fig. 5.4). The measurements of the Hausdorff dimensions confirm that at large scales the universe is genuinely four-dimensional [2]. Most results presented in this pa-

per were obtained for a point that is firmly placed in the phase  $C$  (cf. Fig. 5.3). A typical configuration has a finite time extent and spatial extent which scales as expected for a four-dimensional object. The averaged distribution of a spatial volume coincides with the distribution of Euclidean de Sitter space  $S^4$  and thus this phase is also called the de Sitter phase.

The transitions between phases have been studied in detail in [20]. So far, there is a strong numerical evidence that the transition between phases  $A$  and  $C$  is of first order, while between phases  $B$  and  $C$  there is a second-order transition.

For the  $A$ – $C$  phase transition, the distribution of values taken by the order parameter  $N_0$ , conjugate to  $K_0$ , reveals a two-peak structure, which corresponds to different types of geometry. The peaks become sharper with the increase of the system size,  $N_4 \rightarrow \infty$ . This confirms that configurations behave as if they were either in phase  $C$  or phase  $A$  and suggests that the  $A$ – $C$  transition is of first order.

A similar two-peak distribution of the order parameter conjugate to the coupling constant  $\Delta$ , namely  $N_{41} - 6N_0$ , is present for the  $B$ – $C$  phase transition. But with the increasing total volume  $N_4$  peaks become blurred and start to merge. Also, the measured value of the shift exponent  $\tilde{\nu} = 2.51(3)$  [20] is far from  $\tilde{\nu} = 1$  expected for a first-order transition. The above arguments strongly suggest that the  $B$ – $C$  phase transition is of second order.

## 5.3 The Macroscopic de Sitter Universe

We start the quantitative description of the Universe emerging in causal dynamical triangulations by passing over local degrees of freedom of the quantum geometry, and reducing the considerations to volumes of spatial slices. The causality condition is ensured by imposing on configurations a global proper-time foliation and keeping the topology of leaves fixed. Due to the discrete structure, successive spatial slices, i.e., hypersurfaces of constant time, are labeled by a discrete time parameter  $i$ . The index  $i$  ranges from 1 to  $T$ . By construction, they are glued in the way to form a simplicial manifold with the topology of a three-sphere  $S^3$ .

### 5.3.1 The Spatial Volume

The spatial three-volume  $N(i)$  is defined as the number of tetrahedra constituting a spatial slice  $i = 1, \dots, T$ . Because each spatial tetrahedron is a base of one simplex of the type  $\{1, 4\}$  and one of the type  $\{4, 1\}$ , the three-volumes  $N(i)$  sums up to the total volume  $N_{\text{tot}} \equiv \sum_{i=1}^T N(i) = N_{41}/2$ . The spatial volume  $N(i)$  is an example of the simplest observable providing information about the large-scale shape of the universe appearing in CDT path integral. An individual space-time history contributing to the partition function is not an observable, precisely in the same way as a trajectory of a particle in the quantum-mechanical path integral is not an observable



either. However, it is perfectly legitimate to talk about the expectation value  $\langle N(i) \rangle$  as well as about the fluctuations around the mean.

The lattice regularization present in CDT allows to adapt powerful Monte Carlo techniques to calculate expectation values, defined by Eq. (5.8). Though in two dimensions we have analytical tools, in four dimensions it is currently the only way to extract non-perturbative information about fluctuating geometries. Numerical simulations consist in generating a sequence of space-time geometries, more precisely causal triangulations  $\mathcal{T}$ , according to the probability distribution (5.8). Configurations are then used to calculate the average. A significant feature of the CDT approach, as shown in [11], is a dynamically emerging and physically realistic background geometry, described by the average  $\langle N(i) \rangle$ .

Let us focus on one particular point of the phase diagram firmly placed in phase *C*, and given by the following values of bare coupling constants:  $K_0 = 2.2$ ,  $\Delta = 0.6$ , volume  $N_{41} = 160,000$  and time-period  $T = 80$ . In this phase, the plot of  $N(i)$  for an individual configuration is bell-shaped with a well-outlined *blob*. Figure 5.5 shows the volume profile  $N(i)$  of a typical configuration. For the range of discrete volumes  $N_4$  under study, the Universe *does not* extend over the entire axis, but rather is localized in a region much shorter than  $T = 80$  time slices.

The Einstein–Hilbert action (5.1), and consequently the Regge action (5.4), is invariant under time translations  $t \rightarrow t + \delta$ . Because configurations are periodic in time, a straightforward average  $\langle N(i) \rangle$  is meaningless, as it would give a uniform distribution. From Fig. 5.5 it is clear that in phase *C* the time translation symmetry is *spontaneously broken*. To perform a meaningful average of the spatial volume  $\langle N(i) \rangle$ , we thus fix the position of the center of mass of the volume distribution to be at  $t = 0$ . We apply this procedure to each configuration contributing to the expectation value.

The expectation value  $\langle N(i) \rangle$  is measured using Monte Carlo techniques,

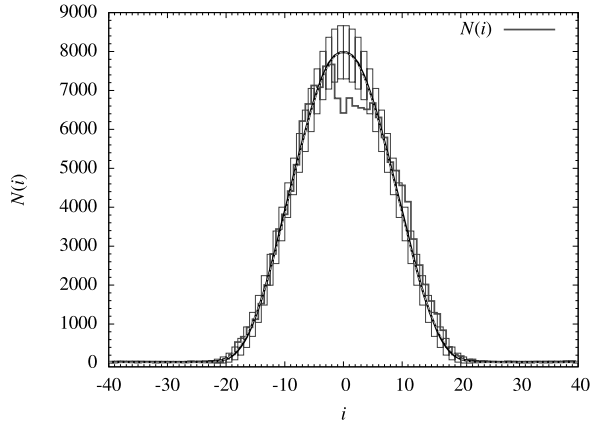
$$\langle N(i) \rangle \approx \frac{1}{K} \sum_{k=1}^K N^{(k)}(i), \quad (5.9)$$

where the brackets  $\langle \dots \rangle$  mean averaging over the whole ensemble of causal triangulations weighted with the Regge action (5.4) and the expectation value is approximated by a sum over  $K$  statistically independent Monte Carlo configurations. Figure 5.5 shows the average spatial volume  $\langle N(i) \rangle$  (black thick line) measured at a point in the phase *C*,  $K_0 = 2.2$  and  $\Delta = 0.6$ . The heights of the boxes visible in the plot indicate the amplitude of spatial volume fluctuations for each  $i$  given by  $\sigma_i = \sqrt{\langle N(i)^2 \rangle - \langle N(i) \rangle^2}$ . Results obtained by simulations show that the average geometry, in the blob and tail region, is extremely well approximated by the formula

$$\bar{N}(i) \equiv \langle N(i) \rangle = H \cdot \cos^3(i/W), \quad (5.10)$$

where  $W$  is proportional to the time extent of the Universe and  $H$  denotes its maximal spatial volume. The fit  $H \cdot \cos^3(i/W)$  is also plotted in Fig. 5.5 with a dashed gray line, but it is indistinguishable from the empirical curve. The background geometry given by the solution (5.10) is consistent with the geometry of a four-sphere

**Fig. 5.5** Spatial volume  $N(i)$  of a randomly chosen typical configuration (gray line) and background geometry  $\langle N(i) \rangle$  (black line): Monte Carlo measurements for fixed  $N_{41} = 160,000$ ,  $K_0 = 2.2$ ,  $\Delta = 0.6$ . The best fit (5.10) yields indistinguishable curves at given plot resolution. The bars height indicate the average size of quantum fluctuations



$S^4$  and corresponds to Euclidean de Sitter space, the maximally symmetric solution of classical Einstein equations with a positive cosmological constant [12, 13].

This is one of the most important results obtained within the CDT framework [11]. While no background was put by hand, the measurements present a direct evidence that the *background geometry* of a four-sphere emerges dynamically. Moreover, neglecting the stalk, which by construction has a non-zero volume, we spontaneously end up with the  $S^4$  topology, although we started with  $\mathcal{M} = S^1 \times S^3$ .

### 5.3.2 The Mini-superspace Model

The shape of the three-volume  $\bar{N}(i) = H \cdot \cos^3(i/W)$  emerges as a classical solution of the *mini-superspace* model. This model appears for example in quantum cosmological theories developed by Hartle and Hawking in their semi-classical evaluation of the wave function of the Universe [17]. This model assumes a spatially homogeneous and isotropic metric on a Euclidean space-time with  $S^1 \times S^3$  topology,

$$ds^2 = d\tau^2 + a^2(\tau)d\Omega_3^2, \quad (5.11)$$

where  $a(\tau)$  is the *scale factor* depending on the *proper time*  $\tau$  and  $d\Omega_3^2$  denotes the line element on  $S^3$ . This means that all degrees of freedom except the three-volume (scale factor) are *frozen*. In CDT model we have the opposite situation, no degrees of freedom are excluded, instead we integrate out all of them but the scale factor. Nevertheless, in both cases results demonstrate high similarity. The *physical volume* of a spatial slice for a given time  $\tau$  equals  $v(\tau) = \int d\Omega_3 \sqrt{\det g|_{S^3}} = 2\pi^2 a(\tau)^3$ . The Euclidean version of the Einstein–Hilbert action (5.1) [5, 6] calculated for the metric (5.11) up to boundary terms is given by

$$S[a] = \frac{2\pi^2}{16\pi G} \int d\tau (-6a\dot{a}^2 - 6a + 2\Lambda a^3), \quad (5.12)$$

and is called the mini-superspace action.

Although it is formally easy to perform the Wick rotation of the Einstein–Hilbert action (5.1), the corresponding Euclidean action suffers from the unboundedness of the conformal mode. This is caused by the wrong sign of the kinetic term, as is reflected in the standard mini-superspace action (5.12). Consequently, the Regge action (5.4) is also unbounded from below. Some triangulations may have very large negative values of the Regge action, but the action is always bounded from below due to the UV lattice regularization. The problem of infinities is revived when taking the continuum limit. Fortunately, in the non-perturbative approaches, like CDT, the partition function emerges as a subtle interplay of the entropic nature of triangulations and the *bare* action. The entropy factor may suppress the unbounded contributions coming from the conformal factor. There is a strong evidence [21] that, after integrating out all degrees of freedom except the scale factor, which means taking into account the non-perturbative measure, one obtains a *positive* kinetic term in (5.12). This is exactly what happens in four-dimensional causal dynamical triangulations: the *effective* action for  $N(i)$  is equal to the mini-superspace action (5.12), but with an opposite sign, and is thus bounded from below. Together with a convergence of the coupling constants to their critical values, if such a point exists, the *entropic* and *action* terms should be balanced, and one hopes to obtain the proper continuum behavior.

Turning back to the spatial volume variable, the mini-superspace action (5.12) can be rewritten as

$$S[v] = -\frac{1}{24\pi G} \int d\tau \left( \frac{\dot{v}^2}{v} + \beta v^{1/3} - 3\Lambda v \right), \quad \beta = 9(2\pi^2)^{2/3}. \quad (5.13)$$

The overall sign of the action does not affect the classical solution of equations of motion. The classical trajectory, solving the Euler–Lagrange equation, is given by

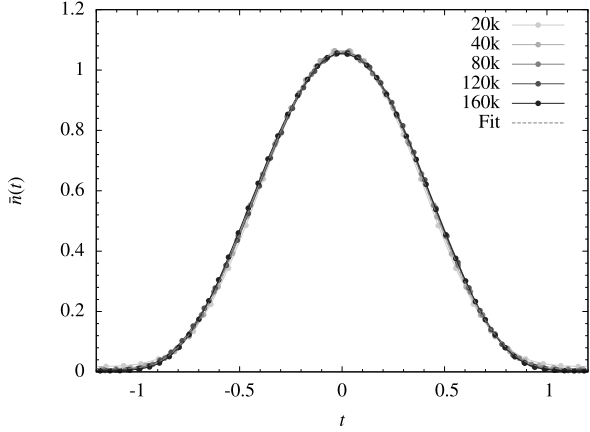
$$\bar{v}(\tau) = 2\pi^2 R^3 \cos^3\left(\frac{\tau}{R}\right), \quad R = \left(\frac{\Lambda}{3}\right)^{-1/2}. \quad (5.14)$$

The physical volume  $\bar{v}(\tau)$  describes the maximally symmetric space for a positive cosmological constant, namely the Euclidean *de Sitter Universe* or a geometry of a four-sphere  $S^4$  with radius  $R$ . This result is in agreement with the relation (5.10) for  $\bar{N}(i)$  found in numerical simulations. The de Sitter space *emerges dynamically* as a background geometry in the CDT model.

### 5.3.3 The Four-Dimensional Space-Time

The scaling properties and the measured spectral dimension of the ensemble of triangulations show that the Universe coming out in the CDT model is genuinely four-dimensional. Up to now, we have presented results for only one value of the total volume  $N_{\text{tot}}$ . Keeping the coupling constants  $K_0$  and  $\Delta$  fixed, which naively means that the geometry of simplices is not changed, we measure the expectation value  $\bar{N}(i)$  for different total volumes  $N_{\text{tot}}$ .

**Fig. 5.6** Average scaled spatial volume  $\bar{n}(t)$  for a variety of total volumes  $N_{\text{tot}}$  calculated for the scaling dimension  $d_H = 4$ . Measured in Monte Carlo simulations for  $K_0 = 2.2$  and  $\Delta = 0.6$ . We omit the error bars not to obscure the picture. The *dashed line* plots the fit  $\bar{n}(t) = \frac{3}{4B} \cos^3(t/B)$ , where  $B = 0.69$



If the scaling dimension is  $d_H$  time intervals should scale as  $N_{\text{tot}}^{1/d_H}$ , which implies that the volume-independent time coordinate  $t$  scales as a function of a discrete time  $i$  as

$$t \equiv \Delta t \cdot i, \quad \Delta t \equiv N_{\text{tot}}^{-\frac{1}{d_H}}. \quad (5.15)$$

To compare the spatial volume distributions  $N(i)$  for geometries with different volumes  $N_{\text{tot}}$ , we introduce the scaled three-volume  $n(t)$ ,

$$n(t) \equiv N_{\text{tot}}^{-1+\frac{1}{d_H}} N(i), \quad \bar{n}(t) = \langle n(t) \rangle. \quad (5.16)$$

For very large  $N_{\text{tot}}$ , the time interval  $\Delta t$  is close to zero and in the continuum limit the sum over discrete time steps can be replaced by an integral,

$$\int dt \dots \leftrightarrow \sum_i \Delta t \dots \quad (5.17)$$

The normalization condition reads  $\int n(t) dt = N_{\text{tot}}^{-1} \sum_i N(i) = 1$ .

Now it is possible to directly compare  $n(t)$  for various total volumes and check for which value of the scaling dimension  $d_H$  the overlap is the best [2]. The estimated value of  $d_H = 3.98 \pm 0.10$  minimizes the error function defined as a spread of scaled spatial volumes  $n(t)$ . The error of determination of  $d_H$  was estimated using the Jackknife method [18]. The expected value  $d_H = 4$  is very close to the measured result, and is well within the margin of error. Figure 5.6 shows the scaled three-volumes  $n(t)$  using  $d_H = 4.0$  for several values of total volumes  $N_{\text{tot}}$ .

Since  $\bar{n}(t)$  is normalized and is obtained by the scaling of  $\bar{N}(i)$  which is given by Eq. (5.10), it is expressed by the formula

$$\bar{n}(t) = \frac{3}{4B} \cos^3\left(\frac{t}{B}\right), \quad (5.18)$$

where  $B$  depends only on the coupling constants  $K_0$  and  $\Delta$ , but not on  $N_{\text{tot}}$ . For  $K_0 = 2.2$  and  $\Delta = 0.6$ , the measured values is  $B \approx 0.69$ . The curve (5.18) with adjusted  $B$  is drawn with a dashed line in Fig. 5.6, and the fit is remarkably good.

From Eqs. (5.16) and (5.18) and the scaling dimension  $d_H = 4$  we obtain the following expression for the three-volume  $\bar{N}(i)$ :

$$\bar{N}(i) = \frac{3}{4} \frac{N_{\text{tot}}^{3/4}}{B} \cos^3 \left( \frac{i}{BN_{\text{tot}}^{1/4}} \right). \quad (5.19)$$

As expected for a four-dimensional space-time, the time extent  $T_{\text{univ}}$  of the blob, measured in units of time steps, scales as  $T_{\text{univ}} \sim \pi B \cdot N_{\text{tot}}^{1/4}$ . The expression (5.19) specifies expression (5.10) and is only valid in the extended part of the Universe where the spatial three-volumes are larger than the minimal cut-off size.

Let us relate the discrete spatial volume  $N(i)$  with the physical volume  $v(\tau)$  of hypersurfaces of constant time. The classical solution  $\bar{v}(\tau)$  is given by formula (5.14), while the average discrete volume  $\bar{N}(i)$  is given by formula (5.19). Up to some factors they are expressed by the same function. Henceforth, we make the key assumption that the average configuration described by  $\bar{N}(i)$  in fact has a geometry of a four-sphere  $S^4$  given by  $\bar{v}(\tau)$ . The physical total four-volume of a four-sphere with a radius  $R$  equals

$$V_4 = \int_{-\frac{\pi}{2}R}^{\frac{\pi}{2}R} \bar{v}(\tau) d\tau = \frac{8\pi^2}{3} R^4 = C_4 a^4 N_{\text{tot}}, \quad (5.20)$$

where

$$C_4 = 2 \left( \text{Vol}^{[4,1]} + \frac{N_{32}}{N_{41}} \text{Vol}^{[3,2]} \right),$$

which is interpreted as the average four-volume shared by one spatial tetrahedron. Here,  $a = a_s$  is the cut-off length, i.e., the lattice constant. The continuum time  $t$  defined by (5.15) and the discrete time  $i$  are proportional to the proper time  $\tau$  (cf. (5.11)),

$$\tau = \sqrt{g_{tt}} t = \sqrt{g_{tt}} \Delta t i, \quad \Delta t = N_{\text{tot}}^{-1/4}. \quad (5.21)$$

A slab between slices  $i$  and  $i + 1$  has a proper-time extent  $\Delta\tau$  and a four-volume

$$v(\tau) \Delta\tau = v(\tau) \sqrt{g_{tt}} \Delta t = C_4 a^4 N(i) = N_{\text{tot}}^{3/4} C_4 a^4 n(t). \quad (5.22)$$

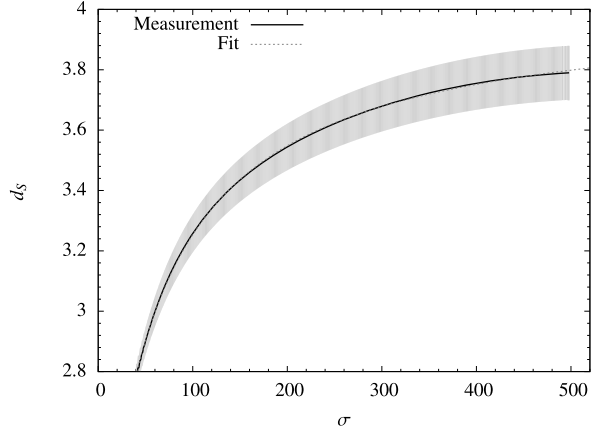
The above equation is consistent with formula (5.20) which determines the total four-volume of the emerging de Sitter space with a radius  $R$ . The proper-time extent of the de Sitter Universe is  $\pi R$ , while in terms of the time  $t$  it is equal to  $\pi B$ , hence

$$\sqrt{g_{tt}} = \frac{\tau}{t} = \frac{R}{B}, \quad R = \left( \frac{3C_4 N_{\text{tot}}}{8\pi^2} \right)^{1/4} a. \quad (5.23)$$

Assuming such scaling relations between physical and discrete volume (cf. (5.22)), and between proper and discrete times (cf. (5.21)), we ensure that the empirically derived formulas (5.18) or (5.19) describe a Euclidean de Sitter Universe for all  $N_{\text{tot}}$ .

Another quantity revealing information about the geometry is related to the diffusion phenomena, namely the so-called spectral dimension  $d_S$ . On a  $d$ -dimensional Riemannian manifold with a metric  $g_{\mu\nu}(\mathbf{x})$ , let  $\rho(\mathbf{x}, \mathbf{x}_0; \sigma)$  be the probability density of finding a diffusing particle at position  $\mathbf{x}$  after some fictitious diffusion time  $\sigma$ ,

**Fig. 5.7** The spectral dimension  $d_S$  of the Universe as a function of diffusion time  $\sigma$ , measured for  $K_0 = 2.2$ ,  $\Delta = 0.6$  and  $N_4 \approx 368k$ . The *thick curve* plots the average measured spectral dimension, while the *highlighted area* represents the error bars. The best fit  $d_S(\sigma) = 4.02 - \frac{120}{58+\sigma}$  is drawn with a *dashed line*



with an initial position at  $\sigma = 0$  fixed at  $\mathbf{x}_0$ . The evolution of  $\rho(\mathbf{x}, \mathbf{x}_0; \sigma)$  is controlled by the diffusion equation

$$\partial_\sigma \rho(\mathbf{x}, \mathbf{x}_0; \sigma) = \Delta_g \rho(\mathbf{x}, \mathbf{x}_0; \sigma), \quad \rho(\mathbf{x}, \mathbf{x}_0; \sigma = 0) = \frac{1}{\sqrt{\det g(\mathbf{x})}} \delta(\mathbf{x} - \mathbf{x}_0), \quad (5.24)$$

where  $\Delta_g$  is the Laplace operator corresponding to  $g_{\mu\nu}(\mathbf{x})$ . The *return probability* describes the probability of finding a particle at the initial point after diffusion time  $\sigma$ . The *average return probability*  $P(\sigma)$ , supplying a global information about the geometries, is given by

$$P(\sigma) = \left\langle \frac{1}{V_4} \int d^d \mathbf{x} \sqrt{\det g(\mathbf{x})} \rho(\mathbf{x}, \mathbf{x}; \sigma) \right\rangle,$$

where  $V_4 = \int d^d \mathbf{x} \sqrt{\det g(\mathbf{x})}$  is the total space-time volume and the average is also performed over the ensemble of geometries. For infinite flat manifolds the spectral dimension  $d_S$  can be extracted from the return probability due to its definition,

$$d_S \equiv -2 \frac{d \log P(\sigma)}{d \log \sigma}. \quad (5.25)$$

For the Euclidean flat manifold  $\mathcal{R}^d$ , the spectral and Hausdorff dimensions are equal to the topological dimension,  $d_S = d_H = d$ . For the four-sphere  $S^4$ , the spectral dimension  $d_S = 4$  for short diffusion times, while for very large times, because of the finite volume, the zero mode of the Laplacian will dominate and, with the above definition,  $d_S$  will tend to zero.

Definition (5.25) is particularly convenient because it is easy to perform numerical simulations which measure the return probability. In the CDT framework, the space-time geometry is regularized by piecewise flat manifolds built of four-simplices. Let us recall that after the Wick rotation space-times appearing in the model are Riemannian manifolds equipped with the positive-definite metric tensor. The diffusion process can be carried out by implementing the discretized version of

the diffusion equation (5.24),  $\rho(i, i_0; \sigma + 1) - \rho(i, i_0; \sigma) = \Delta \sum_{j \leftrightarrow i} (\rho(j, i_0; \sigma) - \rho(i, i_0; \sigma))$ , where  $\Delta$  denotes the time step and the sum is evaluated over all simplices  $j$  adjacent to  $i$ . Here variables  $i_0, i$  and  $j$  denote labels of simplices. The diffusion process is running on the dual lattice, i.e. the probability flows from a simplex to its neighbors. Since each simplex has exactly five neighbors, it is convenient to set  $\Delta = 1/5$  and the diffusion equation reads  $\rho(i, i_0; \sigma + 1) = \frac{1}{5} \sum_{j \leftrightarrow i} \rho(j, i_0; \sigma)$ .

To evaluate  $\rho(i, i_0; \sigma)$ , we pick an initial four-simplex  $i_0$  lying in the central slice  $i_{CV}$  and impose the initial condition  $\rho(i, i_0; \sigma = 0) = \delta_{i i_0}$ . We iterate the diffusion equation and calculate the probability density  $\rho(i, i_0; \sigma)$  for consecutive diffusion steps  $\sigma$  [10]. Finally, we repeat the above operations for a number of random starting points  $i_0$  ( $K = 100$ ) and calculate the average return probability  $P(\sigma) = \frac{1}{K} \sum_{i_0=1}^K \rho(i_0, i_0; \sigma)$ . In numerical simulations the return probability  $P(\sigma)$  is averaged over a number of triangulations ( $\sim 1,000$ ) and the spectral dimension  $d_S$  is calculated from the definition (5.25). Figure 5.7 shows the spectral dimension  $d_S$  as a function of the diffusion time steps  $\sigma$ , in the range  $40 < \sigma < 500$ . For small values of  $\sigma$  ( $< 30$ ) lattice artifacts are very strong and the spectral dimension becomes irregular. Because of the finite volumes of configurations, for very large  $\sigma$  ( $\gg 500$ ), the spectral dimension  $d_S$  falls down to zero. In the presented range, the measured spectral dimension  $d_S$  is very well expressed by the formula

$$d_S(\sigma) = a - \frac{b}{c + \sigma} = 4.02 - \frac{120}{58 + \sigma}, \quad (5.26)$$

where variables  $a, b$  and  $c$  were obtained from the best fit. As observed, the spectral dimension depends on a diffusion time, and thus it is *scale dependent*. Small  $\sigma$ , means that the diffusion process probes only the nearest vicinity of the initial point. Extrapolation of results gives the *short-distance* limit of the spectral dimension

$$d_S(\sigma \rightarrow 0) = 1.95 \pm 0.10.$$

In the *long-distance* limit the spectral dimension tends to

$$d_S(\sigma \rightarrow \infty) = 4.02 \pm 0.05.$$

The short-range value of the spectral dimension  $d_S = 2$ , much smaller than the scaling dimension  $d_H$ , suggests a fractal nature of geometries appearing in the path integral at short distances. At long distances  $d_S = 4$ , and configurations resemble a smooth manifold. Amazingly, such non-trivial scale dependence of the spectral dimension of the quantum space-time, the same infrared ( $d_S = 4$ ) and ultraviolet ( $d_S = 2$ ) behavior, is also present in Hořava–Lifshitz gravity [16] and in the renormalization group approach [19] (see the article by Reuter and Saueressig in this volume).

## 5.4 Quantum Fluctuations

As we have seen, the dynamically emerging background geometry agrees strikingly well with the solution of the mini-superspace model. By investigating properties of

the semi-classical limit of the lattice approach, we will check if quantum fluctuations around the classical trajectory (5.14) are also correctly described by the effective mini-superspace action (5.13). Nevertheless, it should be clearly stated that these considerations are truly non-perturbative, and take into account both a very important influence of the *entropy factor*, which does not depend on bare coupling constants, as well as the bare action (5.4). Based on numerical data obtained by computer simulations, we construct, within the semi-classical approximation, the effective action describing discrete spatial volume  $N(i)$  and compare it with the mini-superspace action (5.13). The effective action comes into existence because of a subtle interplay between the entropy and the bare action (5.4).

Let us denote the deviation of the three-volume  $N(i)$  from the expectation value  $\bar{N}(i)$  by

$$\eta_i = N(i) - \bar{N}(i).$$

Imitating the path integral approach to quantum mechanics,  $N(i)$  describes the position at discrete time  $i$  of a non-physical particle trajectory, giving a contribution to the partition function. Likewise,  $\eta_i$  is a fluctuation from the classical trajectory  $\bar{N}(i)$ . In the semi-classical approximation, the spatial volume fluctuations  $\eta_i$  are described by a quadratic form  $\mathbf{P}$ , obtained by the quadratic expansion of the effective action around the classical trajectory:

$$S[N = \bar{N} + \eta] \approx S[\bar{N}] + \frac{1}{2} \sum_{i,j} \eta_i \mathbf{P}_{ij} \eta_j + O(\eta^3), \quad (5.27)$$

where the sum is performed over time slices  $i, j = 1, \dots, T$ .

The  $\mathbf{P}$  matrix carries information about quantum fluctuations and may be extracted from numerical data. In analogy to  $\langle N(i) \rangle$  (cf. (5.9)), we measure the covariance matrix  $\mathbf{C}$  of volume fluctuations using Monte Carlo techniques,

$$\mathbf{C}_{ij} \equiv \langle \eta_i \eta_j \rangle \approx \frac{1}{K} \sum_{k=1}^K (N^{(k)}(i) - \bar{N}(i))(N^{(k)}(j) - \bar{N}(j)). \quad (5.28)$$

If the quadratic approximation describes properly quantum fluctuations around the average  $\bar{N}$ , the propagator  $\mathbf{C}$  and the matrix  $\mathbf{P}$  are directly related,  $\mathbf{C}_{ij} = \mathbf{P}_{ij}^{-1}$ .

For numerical convenience the measurements were performed only for triangulations with a fixed total volume  $N_{\text{tot}} \equiv \sum_{i=1}^T N(i)$ . This constraint imposes on the covariance matrix  $\mathbf{C}$  the existence of a zero mode, with corresponding constant eigenvector  $e_j^0 = 1/\sqrt{T}$ , preventing the straightforward inversion of  $\mathbf{C}$ . In order to invert the matrix  $\mathbf{C}$  we project it on the subspace orthogonal to the zero mode  $e^0$  and then perform the inversion. Details of this procedure are described in [12].

After measuring in Monte Carlo simulations the covariance matrix  $\mathbf{C}$ , we get the empirical Sturm–Liouville operator  $\mathbf{P}$  which can be compared with the predictions of the mini-superspace model. The empirical  $\mathbf{P}$  matrix has an expected tridiagonal structure with a high accuracy. The tridiagonal form suggests that the effective action describing fluctuations of  $N(i)$  is quasi-local in time. The action consists of the kinetic part, which couples volumes of successive slices providing the non-zero



subdiagonal elements of  $\mathbf{P}$ , and the potential part, which contributes only to the diagonal.

In [11] it was shown that the effective action corresponds to a discretization of the mini-superspace action (5.13) up to an overall sign. Below we derive a discrete version of the mini-superspace action with reversed sign,

$$S[v] = \int d\tau \left( \alpha \frac{\dot{v}^2}{v} + \beta v^{1/3} - 2\Lambda v \right), \quad (5.29)$$

which later will be compared to the empirical action. We have incorporated the factor  $1/(24\pi G)$  into constants  $\alpha, \beta$  and  $\Lambda$ . The discretization procedure is not unique, but up to the order considered here, all discretizations are equivalent. We substitute the physical volume  $v(\tau)$  with the discrete volume  $N(i)$  which may be treated as a continuous variable inside the blob. The *stalk* region is governed by very strong lattice artifacts, and therefore is not reliably treated in the semi-classical approximation. The standard discretization of the time derivative is  $\dot{v} \rightarrow N(i+1) - N(i)$ , and the kinetic part is written as

$$\alpha \frac{\dot{v}^2}{v} \rightarrow g_1 \frac{(N(i+1) - N(i))^2}{N(i+1) + N(i)}.$$

Because both matrices  $\mathbf{C}$  and  $\mathbf{P}$  are symmetric, the discretized terms also must be symmetric in  $i$  and  $i+1$ . The potential part is discretized straightforwardly,

$$\beta v^{1/3} - 2\Lambda v \rightarrow g_2 N(i)^{1/3} - g_3 N(i).$$

Therefore, a discretized, dimensionless version of action (5.29) is given by

$$S[N] = \sum_i g_1 \frac{(N(i+1) - N(i))^2}{N(i+1) + N(i)} + g_2 N(i)^{1/3} - g_3 N(i). \quad (5.30)$$

Further, we show that the discrete effective action (5.30) describes not only the average  $\bar{N}(i)$  (5.10), what follows from the classical trajectory of Eq. (5.29), but indeed also the measured fluctuations  $\eta(i)$ .

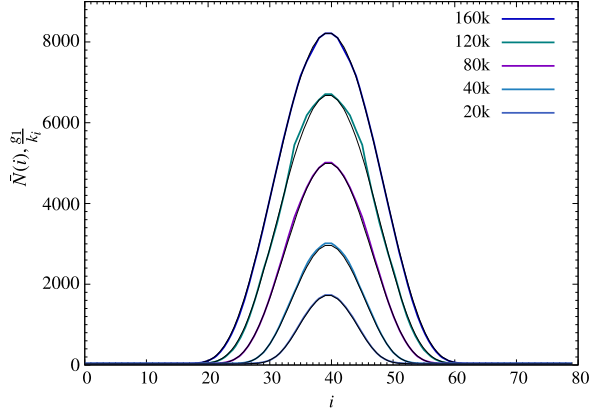
### 5.4.1 The Effective Action

The  $\mathbf{P}$  operator can be decomposed into the *kinetic* part  $\mathbf{P}^{\text{kin}}$  and the *potential* part  $\mathbf{P}^{\text{pot}}$ ,

$$\mathbf{P} = \mathbf{P}^{\text{kin}} + \mathbf{P}^{\text{pot}}.$$

Only the kinetic part  $\mathbf{P}^{\text{kin}}$  contributes to the sub-diagonal elements of the tridiagonal matrix  $\mathbf{P}$ . Because the square of the time derivative couples the preceding and following time steps, and because the covariance matrix is symmetric,  $\mathbf{P}^{\text{kin}}$  should be

**Fig. 5.8** Kinetic term: The directly measured expectation values  $\bar{N}(i)$  (black line), compared to  $\frac{g_1}{k_i}$  (thick line) extracted from the measured covariance matrix  $\mathbf{C}$  for  $K_0 = 2.2$ ,  $\Delta = 0.6$  and various total volumes  $N_{\text{tot}}$  ranging from 20,000 to 160,000 simplices. The theoretical prediction  $\frac{g_1}{k_i} = \frac{1}{2}(\bar{N}(i) + \bar{N}(i+1))$  is realized with a very high accuracy. The value of  $g_1$  is constant for all volumes  $N_{\text{tot}}$



a symmetric tridiagonal matrix, such that the sum of elements in a row or a column is always zero. It can be decomposed into parts linearly dependent on  $k_i$ :

$$\mathbf{P}^{\text{kin}} = \sum_{i=1}^T k_i \mathbf{X}^{(i)}, \quad \mathbf{X}_{jk}^{(i)} = \delta_{ij} \delta_{ik} + \delta_{(i+1)j} \delta_{(i+1)k} - \delta_{(i+1)j} \delta_{ik} - \delta_{ij} \delta_{(i+1)k}, \quad (5.31)$$

where  $\mathbf{X}^{(i)}$  is a matrix corresponding to the discretization of the second time derivative  $\partial_t^2$  at a time  $t = i$ .

Neglecting details of the zero mode removal, the potential part is diagonal,

$$\mathbf{P}^{\text{pot}} = \text{Diag}(\{u_i\}) = \sum_{i=1}^T u_i \mathbf{Y}^{(i)}, \quad \mathbf{Y}_{jk}^{(i)} = \delta_{ij} \delta_{ik}.$$

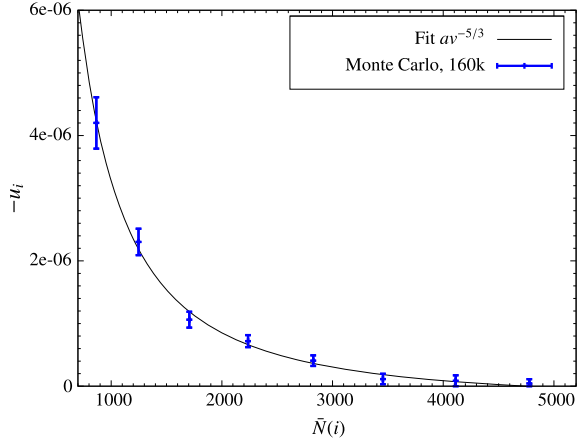
The decomposition of the empirical matrix  $\mathbf{P}$  into a kinetic and potential part is done using the least square method. We find such values of  $\{k_i\}$  and  $\{u_i\}$  for which the matrix  $\mathbf{P}^{\text{kin}} + \mathbf{P}^{\text{pot}}$  is as close as possible to the empirical matrix  $\mathbf{P}$ , i.e., we minimize the residual sum of squares

$$\text{RSS}[\{k_i\}, \{u_i\}] \equiv \text{Tr}[\mathbf{P} - (\mathbf{P}^{\text{kin}} + \mathbf{P}^{\text{pot}})]^2. \quad (5.32)$$

We will omit details of the parameter fitting. Equation (5.32) is quadratic in  $\{k_i\}$  and  $\{u_i\}$ , and the fitting boils down to calculating traces of products of matrices  $\mathbf{X}^{(i)}$  and  $\mathbf{Y}^{(j)}$ . We will show that the fitted values of the kinetic term  $\{k_i\}$ , obtained by minimizing residues (5.32), are indeed in agreement with the kinetic part of the discrete mini-superspace action (5.30). The quadratic expansion (5.27) of the action (5.30) gives

$$k_i = -\mathbf{P}_{ii+1} = -\left. \frac{\partial^2 S[N]}{\partial N(i) \partial N(i+1)} \right|_{N=\bar{N}} = g_1 \frac{8\bar{N}(i)\bar{N}(i+1)}{(\bar{N}(i) + \bar{N}(i+1))^3}. \quad (5.33)$$

**Fig. 5.9** The extracted potential term  $u_i$  as a function of average volume  $\bar{N}(i)$ . The fit  $c_2 \bar{v}_i^{-5/3}$  presents the behavior expected for the mini-superspace model. The visible points correspond to the blob region



In the zeroth order approximation,  $\bar{N}(i) \approx \bar{N}(i+1)$ , we expect the following behavior of the kinetic term:

$$\frac{g_1}{k_i} = \frac{(\bar{N}(i) + \bar{N}(i+1))^3}{8\bar{N}(i)\bar{N}(i+1)} \approx \frac{1}{2}(\bar{N}(i) + \bar{N}(i+1)). \quad (5.34)$$

Figure 5.8 presents the plot of  $g_1/k_i$  for the empirical values of  $k_i$  and various total volumes  $N_{\text{tot}}$ . The theoretical fit (5.34) agrees extremely well with the measured quantities. Additionally, the effective coupling constant  $g_1$  does not depend on  $N_{\text{tot}}$  in the margin of error. For  $K_0 = 2.2$ ,  $\Delta = 0.6$ , we measured  $g_1 = 0.038 \pm 0.002$ . The kinetic part of the quantum fluctuations is indeed described by the mini-superspace action (5.29).

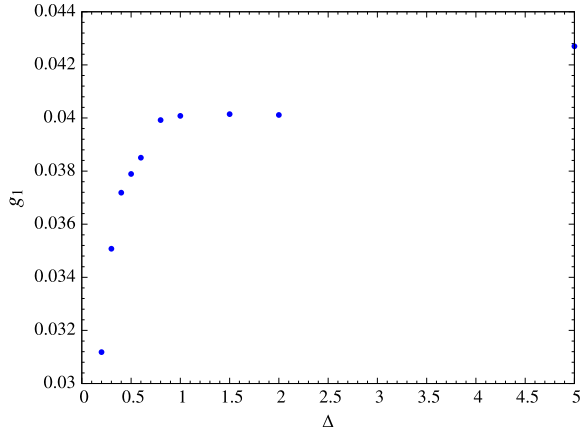
Further we will directly show that values of the potential term  $\{u_i\}$  extracted from the empirical inverse propagator  $\mathbf{P}$  also agree with the mini-superspace model. Within this framework, we expect that

$$u_i = U''(\bar{N}(i)) = -\frac{2}{9}g_2\bar{N}(i)^{-5/3}. \quad (5.35)$$

Figure 5.9 shows the measured values of coefficients  $u_i$  extracted from the empirical matrix  $\mathbf{P}^{\text{pot}}$ . Because of large statistical errors, it is not an easy task to determine  $u_i$ . The physically interesting region of large volumes corresponds to relatively small values of  $u_i$  as they are expected to fall as  $\bar{N}(i)^{-5/3}$ . Due to the existence of the zero mode, the blob region is also affected by the huge contribution from the stalk. Moreover, in analogy with the situation in the ordinary path-integral approach to quantum mechanics, when the time step approaches zero in the continuum limit  $N_{\text{tot}} \rightarrow \infty$ , the potential term is sub-dominant with respect to the kinetic term for individual space-time histories in the path integral.

Nevertheless, due to a sufficiently long Monte Carlo sample, the obtained results allowed us to confirm that indeed Eq. (5.35) is in agreement with measurements. Figure 5.9 presents the measured coefficients  $-u_i$  as a function of the average three-volume  $\bar{N}(i)$ . The error bars shown on the plot were estimated using the Jackknife

**Fig. 5.10** The measured effective coupling constant  $g_1$  as a function of bare coupling constant  $\Delta$  for  $K_0 = 2.2$ . The  $B$ - $C$  transition point is located at about  $\Delta^{\text{crit}} = 0.05$ . When approaching phase  $B$  from phase  $C$ , the coupling constant  $g_1$  diminishes and the fluctuations grow, as expected when reaching phase transition point



method. Such a form allows us to directly compare the potential coefficients with theoretical predictions  $-u_i \propto \bar{N}(i)^{-5/3}$ . The selected range of  $\bar{N}(i)$  corresponds to the *bulk*. The best fit of the form  $f(x) = a x^{-c}$  to the empirical values  $u_i$  as a function of  $\bar{N}(i)$  gives  $c = -1.658 \pm 0.096$ . The measured exponent coefficient  $c$  is very close to the theoretical value  $c = -5/3$ . The fit  $f(x) = a x^{-5/3}$ , corresponding to the potential part of action (5.30), is presented in Fig. 5.9 with a thin line. The agreement with the data is good; the potential part of the effective action is indeed given by  $U(x) = g_2 x^{1/3} - g_3 x$ . Apart from obtaining the correct power  $u_i \propto \bar{N}^{-5/3}(i)$ , the coefficient in front of this term is also independent of  $N_{\text{tot}}$ .

### 5.4.2 Flow of the Gravitational Constant

The quantum fluctuations of the three-volume are very accurately described by the discrete, dimensionless effective action

$$S[N(i)] = \sum_i g_1 \frac{(N(i+1) - N(i))^2}{2N(i)} + g_2 N^{1/3}(i), \quad (5.36)$$

where we have omitted the cosmological constant term, since during the measurements the total volume  $N_{\text{tot}}$  was fixed. This action comes out as a discretization of the mini-superspace action (5.13) with the opposite sign, which solves the problem of unboundedness. Let us note that it is justified to use the semi-classical approximation as the distribution of spatial volumes  $N(i)$  in the bulk is given by Gaussian fluctuations around the mean.

Using Eqs. (5.16), (5.17) and (5.21)–(5.23), we can rewrite the above discrete action in terms of the physical volume  $v(\tau)$ ,

$$S[v(\tau)] = \frac{g_1 g_{II}}{2\sqrt{N_{\text{tot}}} C_4 a^4} \int d\tau \left[ \frac{\dot{v}^2}{v} + \tilde{g}_2 v^{1/3} \right]. \quad (5.37)$$

It is natural to identify the coupling constant  $G$  multiplying the effective action (5.13) with Newton's gravitational constant  $G$ . Using Eq. (5.23), we get the following relations between the gravitational constant  $G$  and the effective constant  $g_1$  [11, 12]:

$$G = \frac{2\sqrt{N_{\text{tot}}}C_4a^4}{24\pi g_1 g_{tt}} = \frac{a^2}{g_1} \frac{\sqrt{C_4}B^2}{3\sqrt{6}}. \quad (5.38)$$

In order to keep fixed the physical constant  $G$ , and thus the amplitude of fluctuations  $\sqrt{\langle(\delta v(\tau))^2\rangle} \propto g_1^{-1/2}N_{\text{tot}}^{1/4}a^2$ , when taking the continuum limit  $a \rightarrow 0$  one has to tune the effective coupling constant  $g_1 \propto a^2$ . This means that in terms of the lattice volume  $N(i)$  fluctuations should diverge, and this happens when we approach a second- or higher-order transition line. Therefore it is important to determine the order of the transition. Figure 5.10 shows the measured effective coupling constant  $g_1$  for various values of  $\Delta$ . As mentioned before, the effective coupling constant  $g_1$  does not depend on  $N_{\text{tot}}$  when the bare coupling constants are fixed, and the same is true for the classical trajectory  $\bar{v}(t)$ . Therefore, one also has to properly tune the bare coupling constants so that the *effective* coupling constant satisfies  $g_1a^{-2} = \text{const}$  while taking the limits  $N_{\text{tot}} \rightarrow \infty$  and  $a \rightarrow 0$ . Indeed, when we approach the  $B$ – $C$  transition line  $g_1$  tends to zero.

Using relation (5.38) we can express the cut-off length  $a$  in terms of the Planck length, and thus estimate the size of the Universe generated in computer simulations. Let us recall that in natural units  $G = \ell_{\text{Pl}}^2$ . For the bare coupling constants  $K_0 = 2.2$ ,  $\Delta = 0.6$  we measured the quantities:  $K_4^{\text{crit}} = 0.922$ ,  $\xi = N_{32}/N_{41} = 1.30$ ,  $\alpha = 0.5858$ ,  $C_4 = 0.0317$ ,  $g_1 = 0.038$ , which results in  $a \approx 1.9\ell_{\text{Pl}}$  and the linear size  $\pi R$  of the universe built from 160,000 simplices is about  $20\ell_{\text{Pl}}$ . The quantum de Sitter universes studied here are therefore quite small, and quantum fluctuations around their average shape are large (cf. (5.5)). Surprisingly, the semi-classical mini-superspace formulation gives an adequate description of the measured data, at least for the volume profile.

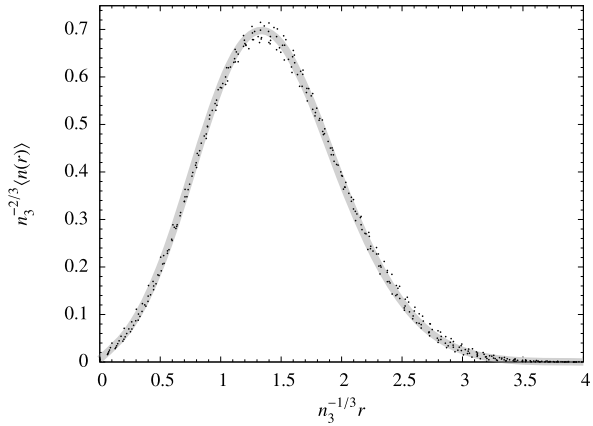
## 5.5 The Geometry of Spatial Slices

Let us look deeper into the geometry of spatial slices. A spatial slice is a leaf of the imposed global proper-time foliation and is labeled by a discrete time index  $i$ . Each such hypersurface is a three-dimensional triangulation built of equilateral spatial tetrahedra, more precisely, a piecewise linear manifold of topology  $S^3$ . However, it does not mean that the geometry of slices is close to the geometry of a three-dimensional sphere.

### 5.5.1 The Hausdorff Dimension

Let us denote the number of tetrahedra building slice  $i$  by the discrete three-volume  $n_3 \equiv N(i)$ . A basic observable defined on a slice is the number of tetrahedra  $n(r, i_0)$

**Fig. 5.11** Scaled values of the radius  $n_3^{-1/d_H} r$  and shell area  $n_3^{-1+1/d_H} n(r)$  for  $d_H = 3$ . Data points for various values of slice volume  $n_3$  overlap. The *gray strip* plots the scaled radial volume averaged over all data points. Measurements were performed at  $K_0 = 2.2$  and  $\Delta = 0.6$



at a three-dimensional distance  $r$  from some initial tetrahedron  $i_0$ . At distance  $r = 0$  only the initial tetrahedron is counted and  $n(0, i_0) = 1$ . For such definition,  $n(r, i_0)$  corresponds to an area of the shell of radius  $r$ . Summing up the area over all shells gives the discrete volume of a slice  $n_3$ . Let  $n(r)$  denotes the average of  $n(r, i_0)$  over all  $n_3$  initial tetrahedra  $i_0$ ,

$$n(r) = \frac{1}{n_3} \sum_{i_0=1}^{n_3} n(r, i_0), \quad n_3 = \sum_{r=0}^{r_{max}} n(r, i_0).$$

We will investigate scaling properties of  $n(r)$  with respect to the slice volume  $n_3$ . The Hausdorff dimension of spatial slices may be measured by a comparison of the scaled with volume  $n_3$  values of the radial volume  $n(r)$ . First, for a large number of Monte Carlo configurations, slices with the same volume  $n_3$  (more or less few tetrahedra) are collected into groups. The average radial volume  $n(r)$  within a group  $n_3$  is denoted as  $\langle n(r) \rangle_{n_3}$ .

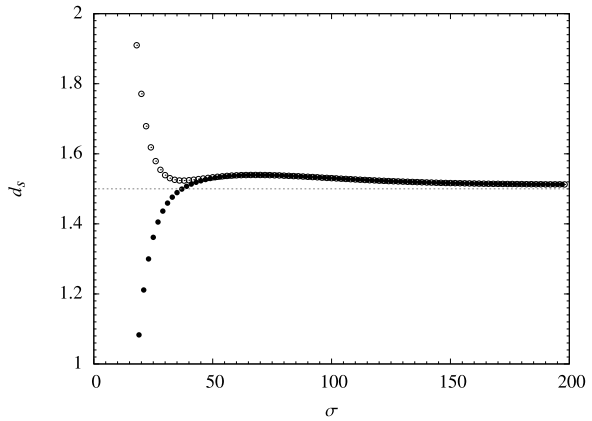
For the Hausdorff dimension  $d_H$  we expect that the radius  $r$  and the average volume  $\langle n(r) \rangle_{n_3}$  scaled and normalized in the following way

$$(r, \langle n(r) \rangle_{n_3}) \rightarrow (n_3^{-1/d_H} r, n_3^{-1+1/d_H} \langle n(r) \rangle_{n_3}) \quad (5.39)$$

overlap for all  $n_3$ . We define the error of the overlap of the scaled points and find such value of  $d_H$  which minimizes the dispersion. The best fit is obtained for  $d_H = 2.94 \pm 0.05$ . Figure 5.11 presents the measured values of  $\langle n(r) \rangle_{n_3}$  scaled according to (5.39) with  $d_H = 3$  and for various values of  $n_3$  between 1,000 and 4,000 tetrahedra.

The measured value of  $d_H$  is independent of the coupling constants  $K_0$  and  $\Delta$ , as long as we stay well inside the phase  $C$ . This results is true if we consider the ensemble average of the slice geometry, but it does not mean that individual spatial slices resemble a smooth three-dimensional geometry.

**Fig. 5.12** Spectral dimension  $d_S$  of spatial slices as a function of diffusion time  $\sigma$ . For short diffusion times, a split for even (*empty*) and odd (*filled*) values of  $\sigma$  is observed arising from the discrete structure. The measured values of  $d_S$  converge to the thin line corresponding to  $d_S = 1.5$



### 5.5.2 Spectral Dimension

We measure the spectral dimension of spatial slices in the same way as for the whole simplicial manifolds. The probability of finding a diffusing particle in tetrahedron  $i$  after a diffusion time  $\sigma$  and starting at tetrahedron  $i_0$  is given by the probability density  $\rho(i, i_0; \sigma)$ . The discrete diffusion equation, describing the evolution of the probability density, can be written as  $\rho(i, i_0; \sigma + 1) = \frac{1}{4} \sum_{j \leftrightarrow i} \rho(j, i_0; \sigma)$ , where the sum is over all tetrahedra  $j$  adjacent to  $i$ . For a starting tetrahedron  $i_0$ , chosen at random, we set the initial condition  $\rho(i, i_0; \sigma = 0) = \delta_{i i_0}$ . By iterating the diffusion equation, we calculate the return probability  $P(\sigma, i_0) \equiv \rho(i_0, i_0; \sigma)$  for successive discrete diffusion steps  $\sigma$ . Further, we compute the *average return probability*  $P(\sigma) \equiv \langle \langle P(\sigma, i_0) \rangle \rangle_{i_0} MC$  by averaging over initial points and configurations. For each configuration we consider only the central slice. The spectral dimension  $d_S$  is obtained from the return probability using the definition (5.25). For a three-sphere geometry, the spectral dimension  $d_S$  is equal 3 for short diffusion times, and  $d_S$  will tend to zero for longer times. Figure 5.12 shows the values of the spectral dimension  $d_S$  as a function of the diffusion time  $\sigma$ , determined by numerical simulation using the definition (5.25) for a randomly chosen typical configurations in phase C. Due to the discrete lattice structure, for small values of  $\sigma$  a split for even and odd diffusion times is observed. Because of the finite volumes of the spatial slices, for very large  $\sigma$ ,  $d_S$  falls down to zero. For the intermediate region, there is a plateau of the spectral dimension at  $d_S \approx 1.5$ .

The significant difference between the measured Hausdorff dimension of spatial slices,  $d_H \approx 3$ , and the measured spectral dimension,  $d_S \approx 1.5$ , is an indication of the fractal nature of the slices. Indeed, this was proved in a direct way [14]. The three-dimensional spatial slices reveal a large number of *minimal necks*. A minimal neck consists of four triangles forming a tetrahedron, but where this tetrahedron does not belong to the triangulation. They provide the three-dimensional triangulation with a tree-structure (for  $S^3$  geometry). At many random places, a branch bifurcates into two or more branches. Most probably when the size of the slice grows

to infinity, we would observe the fractal structure of branched polymers. A similar structure is present in three-dimensional Euclidean dynamical triangulations, where so-called *baby Universes* separated by minimal necks are observed [22].

## 5.6 Conclusions

The model of causal dynamical triangulations is a non-perturbative and background-independent approach to quantum gravity. The foundations of this model are very simple. It is a mundane lattice field theory with a piecewise linear manifold serving as a regularization of general relativity. The introduction of Wick rotation allows us to use very powerful Monte Carlo techniques and calculate quantum expectation values of observables.

Based on the Monte Carlo measurements we predict the existence of three phases within the CDT model. In the physically most interesting phase, so called de Sitter phase, the time-translational symmetry is spontaneously broken and the scale factor as a function of time behaves as a bell-shaped distribution. Recent results give a strong evidence that the Universe which emerges dynamically in causal dynamical triangulations is genuinely *four-dimensional*. Its geometry corresponds to de Sitter space, the maximally symmetric solution to the classical Einstein equations in the presence of a positive cosmological constant. At large scales both the Hausdorff and spectral dimensions are equal to 4. CDT presents a picture of the Universe with superimposed finite quantum fluctuations around the classical trajectory, which are well described semi-classically. The measurements of the covariance matrix allowed us to reconstruct the discrete effective action describing quantum fluctuations of the three-volume  $N(i)$ . This action was identified with the discretization of the mini-superspace action. In the CDT model, however, no reduction of degrees of freedom is introduced. Due to the identification, the effective coupling constant can be related to the physical gravitational constant, giving a recipe of how to obtain a meaningful continuum limit and expressing the lattice constant in terms of physical units.

The spatial slices of the imposed foliation reveal, however, a fractal structure similar to branched polymers. Although the measurements show that the Hausdorff dimension of the slices is equal to 3, the measured spectral dimension is only half of this value. Indeed, the fractality was confirmed by a direct analysis of tree structures defined in terms of so-called minimal necks.

**Acknowledgements** The author would like to thank Jerzy Jurkiewicz and Jan Ambjørn for introducing him into this fascinating topic and for a fruitful collaboration. The author acknowledges support by *The Danish Research Council* via the grant “Quantum Gravity and the Role of Black Holes”.

## References

1. J. Ambjørn, J. Jurkiewicz, R. Loll, Phys. Rev. Lett. **85**, 924 (2000). [hep-th/0002050](https://arxiv.org/abs/hep-th/0002050)



2. J. Ambjørn, J. Jurkiewicz, R. Loll, Phys. Rev. D **72**, 064014 (2005). [hep-th/0505154](#)
3. J. Ambjørn, J. Jurkiewicz, R. Loll, Nucl. Phys. B **610**, 347 (2001). [hep-th/0105267](#)
4. J. Ambjørn, J. Jurkiewicz, R. Loll, in *Approaches to Quantum Gravity*, ed. by D. Oriti (Cambridge University Press, Cambridge, 2009), pp. 341–359. [hep-th/0604212](#)
5. S.W. Hawking, in *General Relativity: An Einstein Centenary Survey*, ed. by S.W. Hawking, W. Israel (Cambridge University Press, Cambridge, 1979), pp. 746–789
6. G.W. Gibbons, S.W. Hawking, Phys. Rev. D **15**, 2752 (1977)
7. C.W. Misner, K.S. Thorne, J.A. Wheeler, *Gravitation* (Freeman, New York, 1973)
8. R.M. Wald, *General Relativity* (Chicago University Press, Chicago, 1984)
9. J. Ambjørn, S. Varsted, Nucl. Phys. B **373**, 557 (1992)
10. J. Ambjørn, J. Jurkiewicz, R. Loll, Phys. Rev. Lett. **95**, 171301 (2005). [hep-th/0505113](#)
11. J. Ambjørn, A. Görlich, J. Jurkiewicz, R. Loll, Phys. Rev. Lett. **100**, 091304 (2008). [arXiv:0712.2485](#)
12. J. Ambjørn, A. Görlich, J. Jurkiewicz, R. Loll, Phys. Rev. D **78**, 063544 (2008). [arXiv:0807.4481](#)
13. A. Görlich, Acta Phys. Pol. B **39**, 3343 (2008)
14. J. Ambjørn, A. Görlich, J. Jurkiewicz, R. Loll, Phys. Lett. B **690**, 420 (2010). [arXiv:1001.4581](#)
15. J. Ambjørn, A. Görlich, S. Jordan, J. Jurkiewicz, R. Loll, Phys. Lett. B **690**, 413 (2010). [arXiv:1002.3298](#)
16. P. Hořava, Phys. Rev. Lett. **102**, 161301 (2009). [arXiv:0902.3657](#)
17. J.B. Hartle, S.W. Hawking, Phys. Rev. D **28**, 2960 (1983)
18. B. Efron, Ann. Stat. **7**, 1 (1979)
19. O. Lauscher, M. Reuter, J. High Energy Phys. **0510**, 050 (2005). [hep-th/0508202](#)
20. J. Ambjørn, S. Jordan, J. Jurkiewicz, R. Loll, Phys. Rev. Lett. **107**, 211303 (2011). [arXiv:1108.3932](#)
21. A. Dasgupta, R. Loll, Nucl. Phys. B **606**, 357 (2001). [hep-th/0103186](#)
22. J. Ambjørn, S. Jain, G. Thorleifsson, Phys. Lett. B **307**, 34 (1993). [hep-th/9303149](#)